# Ultra-Massive MIMO Channel Measurements at 5.3 GHz and a General 6G Channel Model

Yi Zheng, Cheng-Xiang Wang, *Fellow, IEEE*, Runruo Yang, Long Yu, Fan Lai, Jie Huang, *Member, IEEE*, Rui Feng, *Member, IEEE*, Chao Wang, Chao Li, and Zhimeng Zhong

***Abstract*—Ultra-massive multiple-input multiple-output (MIMO) technology will bring unique channel characteristics that need to be fully explored through channel measurements and channel modeling. In this paper, single-user and multi-user channel measurements using ultra-massive MIMO antenna arrays with different configurations are conducted at 5.3 GHz band. The non-stationarity, spherical wavefront, channel hardening, and sparse properties are validated by the channel measurements. Correspondingly, a general three-dimensional (3D) sixth generation (6G) non-stationary geometry-based stochastic model (GBSM) for ultra-massive MIMO communication systems is proposed. The statistical properties of channel measurements and the corresponding channel model are studied, including delay power spectral density (PSD), angular PSD, spatial cross-correlation function (SCCF), normalized user-side correlation matrix, singular value spread (SVS), degrees of freedom (DoF), and diversity level. In addition, channel capacities of channel measurements and the corresponding channel model are studied. The accuracy of the proposed general channel model is validated by the consistency of simulation results and measurement results, which indicates that the proposed model can be applied to ultra-massive MIMO communication systems.**

***Index Terms*—Ultra-massive MIMO, channel measurements, channel modeling, channel hardening, channel capacity.**

## I. Introduction

WIth the development of the fifth generation (5G) communication technologies and a variety of services associated with application scenarios, e.g., enhanced mobile broadband (eMBB), massive machine type communications (mMTC), and ultra-reliable low latency communications (uRLLC), the global commercial deployment and evolution towards to sixth generation (6G) communication technologies are in full swing [1], [2]. It is widely believed in the industry that the 6G communication technologies are expected to be commercially available by 2030. One of the evolutions is from massive multiple-input multiple-output (MIMO) to ultra-massive MIMO for enhanced power efficiency and spectral efficiency [3]–[10]. Compared with massive MIMO communication systems, the number of antennas and the dimension of antenna array are further increased in ultra-massive MIMO communication systems, which will bring unique channel characteristics.

To study the characteristics of ultra-massive MIMO channels, it is essential to conduct corresponding channel measurements. In [11], [12], channel measurements were performed in outdoor stadium scenarios at 1.4725 GHz with 91 MHz bandwidth using two array configurations, including a 128 elements virtual uniform linear array (ULA) and a uniform cylindrical array (UCA). The main channel measurement results showed that the angle of departure (AoD) drifts along the ULA and can be fitted by sine curve along UCA, which verified the spherical wavefront. Note that spherical wavefront should be considered in the case that the distance from the transmitter (Tx) to the cluster or the receiver (Rx) is within Rayleigh distance $2{L_A}^2/\lambda$ (near field region). Here, $L_A$ is the largest aperture of antenna array and $\lambda$ is the wavelength of the carrier frequency [13]–[15]. Sangodoyin *et al.* [16], [17] conducted channel measurements in urban scenarios at 2.53 GHz with a bandwidth of 20 MHz using virtual 16×60 antennas UCA at the Tx and a dual polarized 64 ports uniform circular patch array at the Rx. The intra-cluster properties, inter-cluster properties, and correlation of cluster parameters were studied. Gao *et al.* [18]–[21] and Payami *et al.* [22], [23] conducted channel measurements at 2.6 GHz with 50 MHz bandwidth. The base station (BS) was equipped with a 128 ports virtual ULA and a 128 ports UCA or only equipped with a 128 ports virtual ULA. The Rician K-factor, antenna correlation, received power level, average power delay profile (APDP), and root-mean-square (RMS) delay spread (DS) were investigated to prove the non-stationarity in space domain. In addition, the eigenvalue distribution was studied to prove channel hardening property [24]. Spatial non-stationarity brings the disappearance and appearance phenomenon of clusters along the array, which indicates that different antenna

This work was supported by the National Key R&D Program of China under Grant 2018YFB1801101, the National Natural Science Foundation of China (NSFC) under Grants 61960206006, 62271147, and 61901109, the Key Technologies R&D Program of Jiangsu (Prospective and Key Technologies for Industry) under Grants BE2022067 and BE2022067-1, the Frontiers Science Center for Mobile Information Communication and Security, the EU H2020 RISE TESTBED2 project under Grant 872172, the Research Fund of National Mobile Communications Research Laboratory, Southeast University, under Grant 2021B02, the High Level Innovation and Entrepreneurial Doctor Introduction Program in Jiangsu under Grant JSSCBS20210082, the Fundamental Research Funds for the Central Universities under Grant 2242022R10067, the Fellowship of China Postdoctoral Science Foundation under Grant 2021M690628, and the Natural Science Foundation of Shandong Province under Grant ZR2019PF010. ( *Corresponding authors: Cheng-Xiang Wang and Jie Huang*)

Y. Zheng, C.-X. Wang, R. Yang, L. Yu, F. Lai, and J. Huang are with the National Mobile Communications Research Laboratory, School of Information Science and Engineering, Southeast University, Nanjing 210096, China, and also with the Purple Mountain Laboratories, Nanjing 211111, China (email: {zheng_yi, chxwang, yangrr, yulong, lai_fan, j_huang}@seu.edu.cn).

R. Feng is with Purple Mountain Laboratories, Nanjing 211111, China, and also with the School of Information Science and Engineering, Southeast University, Nanjing 210096, China (e-mail: fengxiurui604@163.com).

C. Wang, C. Li, and Z. Zhong are with Huawei Technologies Co., Ltd., Shanghai 310000, China (e-mail: {wangchao307, lichao18, zhongzhimeng}@huawei.com).

elements along the array will see different clusters [25]–[28]. Channel hardening phenomenon (favorable propagation condition) [29]–[31] refers to that with the increase of antenna elements exploited at the BS side, the channels of different users become gradually orthogonal. In [32], [33], channel measurements were conducted at 3.5 GHz with a bandwidth of 200 MHz in urban scenarios and a 32 antenna elements uniform planar array (UPA) was adopted to form a 256 antenna elements virtual array. The channel capacity of the measurement channel is smaller than that of the independent identically distributed channel. It can be concluded that the favorable propagation condition in which the channels between users are orthogonal can not be realized.

All above channel measurements used virtual antenna arrays and the carrier frequencies were typical application frequency bands, such as 1.4725 GHz [11], [12], 2.53 GHz [16], [17], 2.6 GHz [18]–[23], and 3.5 GHz [32], [33]. None of them investigated channel characteristics and system performance comprehensively.

Martínez *et al.* [34], [35] conducted channel measurements with 5.78 m long antenna array at 5.8 GHz with a bandwidth of 100 MHz. The main conclusion was that the correlation between users will become smaller with more antenna elements explored at the BS. The correlation between users was not sufficient for the analysis of comprehensive ultra-massive MIMO channel characteristics.

The characteristics of ultra-massive MIMO may bring new requirements for channel modeling, which is essential in system performance evaluation. However, the existing ultra-massive MIMO channel models either concentrated on characteristic analysis or investigated system performance evaluation in [13], [15], [25]–[27], [36], [37]. None of them studied channel characteristics and the influence on system performance evaluation. Wu *et al.* [25] proposed a twin-cluster geometry-based stochastic model (GBSM) for massive MIMO communication systems to investigate non-stationarity in space domain and time domain and a general channel model [13] to investigate non-stationarity in space-time-frequency (STF) domains. López *et al.* [15] proposed a channel model for a second-order approximation in space domain and time domain of the spherical wavefront, i.e., parabolic wavefront of massive MIMO channel to efficiently model the effects of near-field. Bian *et al.* [27] proposed a general channel model which can be reduced to a massive MIMO channel model and Xie *et al.* [36] proposed a three-dimensional (3D) two-cylinder regular-shaped GBSM for the application requirements of massive MIMO communication systems. Both of them investigated spherical wavefront and non-stationarity in space domain and time domain. Li *et al.* [37] proposed a cluster-based channel model to characterize the spatial non-stationarity. To the best of the authors' knowledge, the general 3D GBSM for ultra-massive MIMO communication systems studying spherical wavefront, STF non-stationarity, channel hardening, spatial consistency, and investigating system performance evaluation is still missing in the literature.

Although the literature mentioned above have conducted plenty of massive MIMO channel measurements [11], [12], [16]–[23], [32]–[35], the ultra-massive MIMO channel measurement using physically large antenna arrays and the corresponding channel model investigating channel characteristics and system performance evaluation are still lacking. In order to fill the gaps mentioned above, we conduct the single-user and multi-user channel measurements in an urban scenario at 5.3 GHz with 160 MHz bandwidth and propose the corresponding channel model for characterizing the channel of ultra-massive MIMO communication systems. The main contributions and novelties of this paper are summarized as follows.

1) The single-user and multi-user channel measurements are conducted using different ultra-massive MIMO antenna configurations at the BS side, including ULA and distributed uniform linear array (DULA). The non-stationarity, spherical wavefront, channel hardening, and sparse properties are validated by the channel measurements.
2) A general 3D GBSM for ultra-massive MIMO communication systems is proposed. The model is suitable for multiple frequency bands and multiple scenarios, including millimeter wave (mmWave), vehicle-to-vehicle (V2V), high-speed train (HST) communications, etc. In addition, the model covers a variety of channel characteristics, including spherical wavefront, channel hardening, spatial consistency, non-stationarity in STF domains, etc.
3) Statistical properties including delay power spectral density (PSD), angular PSD, spatial cross-correlation function (SCCF), normalized user-side correlation matrix, singular value spread (SVS), degrees of freedom (DoF), and diversity level are studied. In addition, the channel capacity is investigated. The simulation results and measurement results are mutually verified, which gives proof of the generality and accuracy of the proposed model.

The rest of this paper is organized as follows. In Section II, we introduce the 5.3 GHz ultra-massive MIMO channel measurements. Section III shows the general ultra-massive MIMO GBSM in details. In Section IV, we present channel measurements and simulation results and analysis. Finally, conclusions are drawn in Section V.

## II. Ultra-massive MIMO Channel Measurements

### A. Time-domain Ultra-massive MIMO Channel Sounder

The channel measurements are conducted at 5.3 GHz with 160 MHz bandwidth using the ultra-massive MIMO channel sounder, which is illustrated in Fig. 1. The Tx side includes a vector signal generator (VSG) which can support the generation and transmission of arbitrary waveforms, e.g., typical pseudo noise (PN) sequence, a power amplifier (PA), a switch matrix which can support 8 or 16 channels in serial, 8 omnidirectional antennas spacing 5 cm with horizontally and vertically polarized arranged alternately, and a GPS Rubidium clock. The Rx side includes a ULA up to 4.3 m with antenna element spacing 0.6 wavelength, 4 switch matrices which can support 4 channels in parallel and 32 channels in serial to totally support 4×32 channel measurements, a switch controller, a low noise amplifier (LNA) with 4 channels, a multi-channel

PXI acquisition system and equipped with a high speed disk array which can support long time data acquisition, and a GPS Rubidium clock. All above equipment and corresponding parameters are summarized in Table I. It is worth mentioning that the ultra-massive MIMO channel sounder supports flexible switch mode, multi-channel sharing local oscillator and phase synchronization, high dynamic range, multi-channel extension, and high speed data transmission that can be used for outdoor ultra-massive MIMO channel measurements.

### B. *Ultra-Massive MIMO Channel Measurements*

Both single-user and multi-user ultra-massive MIMO channel measurements are conducted in an urban scenario at 5.3 GHz with 160 MHz bandwidth. The measurement routes, measurement positions (Tx positions), and the position of ultra-massive MIMO antenna array (Rx position) are shown in Fig. 2. There are 4 measurement routes named as Route 1 (South of China Network Valley A1, Park), Route 2 (South of China Network Valley A1, North of Mozhou East Road, Pavement), Route 3 (East of China Network Valley A1, Keyuan Street), and Route 4 (South of China Network Valley A1, South of Mozhou East Road, Wisdom Jiangning mansion downstairs). There are 42 measurement positions in total, including 17 line-of-sight (LOS) positions shown as stars and 25 non-line-of-sight (NLOS) positions shown as circles. The detailed channel measurement parameters are illustrated in Table II. The channel measurement steps are summarized as follows. First, connect the Tx and Rx directly and set them up to carry out calibration and obtain the response of the measurement equipment. Then, move the Tx to the measurement positions and set up the Tx and Rx to conduct channel measurements. Note that there are two persons walking randomly around the Tx during channel measurements. Finally, by measurement data processing, the channel impulse response (CIR) can be obtained.

*1) Single-user channel measurements:* The single-user channel measurement is performed at inside and outside roads of the China Network Valley. The Tx channel sounder is located on a truck with the antenna height about 1.5 m. Furthermore, the Tx is configured with 8 omnidirectional antennas spacing 5 cm with horizontally and vertically polarized arranged alternately. The Rx channel sounder is located in a small room on the top of the 4th floor with Rx antenna about 20 m high. To compare different array configurations, the Rx antenna array is set to two configurations. One is 4.3 m long linear array with antenna element spacing 0.6 wavelength, which is called ULA and the other is 8-subarray divided from the ULA with subarray spacing 0.4 m to form a linear array with a total length of 7.2 m, which is called DULA. Fig. 3 (a) shows the measurement environment and Figs. 3 (b) and (c) show the ultra-massive MIMO antenna configurations with ULA and DULA, respectively.

*2) Multi-user channel measurements:* The multi-user channel measurement scenario is the same urban scenario as the single-user channel measurement. The difference is that the Tx consists of 4 users with 4 antennas for each user. For each user the 4 antennas are arranged at 4 vertices of the square, one diagonal vertically polarized and the other diagonal horizontally polarized. The center of the square is the Tx channel sounder. The antenna configuration and measurement environment are shown in Fig. 4.

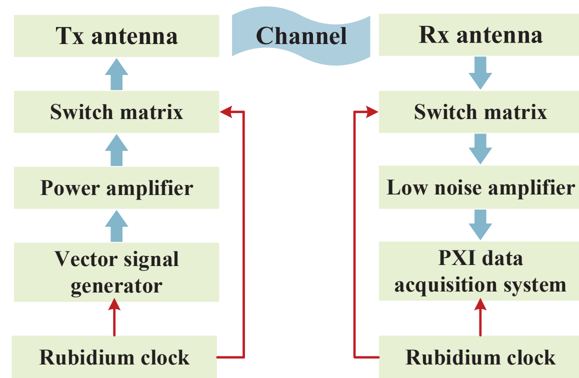


Fig. 1. System chart of the ultra-massive MIMO channel sounder.

TABLE I
EQUIPMENT OF ULTRA-MASSIVE MIMO CHANNEL SOUNDER AND CORRESPONDING PARAMETERS.

| Equipment | Parameters |
|---|---|
| VSG | Frequency range: 9 kHz-6 GHz |
| | Maximum bandwidth: 200 MHz |
| | Maximum output power: 25 dBm |
| PA | Frequency range: 500 MHz-6 GHz |
| | Maximum input power: 0 dBm |
| | Maximum output power: 46 dBm |
| Tx switch matrix | Minimum isolation: 50 dB |
| | Number of channels in serial: 8 or 16 |
| Tx antenna VERT2450 | Gain: 3 dBi |
| | Frequency range: 2.4-2.48 GHz, 4.9-5.9 GHz |
| | Omnidirectional |
| Rubidium clock | Precision: $10^{-13}$ s |
| Rx antenna | Configuration: 128-channel linear array, each channel consists of 8-element omnidirectional patch antenna |
| | Vertical beam width: $12° \pm 2°$ |
| | Horizontal beam width: $85° \pm 4°$ |
| Rx switch matrix | Number of channels in serial: 32 |
| | Minimum isolation: 50 dB |
| LNA | Frequency range: 2-6 GHz |
| | Gain range: 10-60 dB |
| | Number of channels: 4 |
| Multi-channel acquisition system based on PXI | Frequency range: Sub-6 GHz |
| | Maximum sampling rate: 250 MSa/s |
| High speed disk array | Capacity: 4 TB |

### C. *Channel Measurement Data Processing*

*1) Acquisition of CIR:* The CIR can be obtained by system calibration and data processing. The main purpose of system calibration and data processing is to eliminate the response of measurement equipment [38]. Assuming that the transmitted signal is $x(t)$, the received signal is $y(t)$, the response of the measurement equipment is $g(t)$, and the CIR is $h(t)$. Then, by direct calibration, the received signal $y_{th}(t)$ can be obtained as

$$y_{th}(t) = x(t) * g(t) \tag{1}$$

where $*$ represents the time domain convolution operator. The direct calibration received signal $y_{th}(t)$ can be obtained by convolving the transmitted signal $x(t)$ with the response

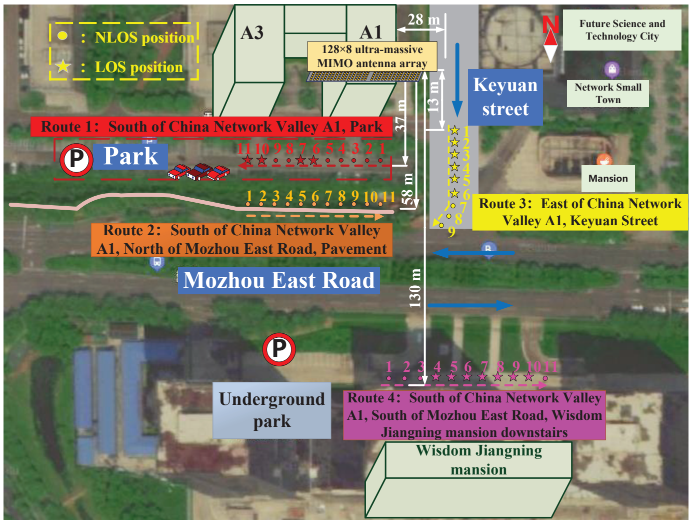


Fig. 2. Measurement routes and positions in an urban scenario.

TABLE II
THE CHANNEL MEASUREMENT PARAMETERS.

| Parameters | Single-user channel measurements | Multi-user channel measurements |
|---|---|---|
| Tx antenna number | 8 | 4 users and 4 antennas for each user |
| Rx antenna number | 128-channel ULA, 8 antennas for each channel; 128-channel DULA, 8 antennas for each channel | |
| Carrier frequency | 5.3 GHz | |
| Bandwidth | 160 MHz | |
| Tx antenna height | 1.5 m | |
| Rx antenna height | 20 m | |

of the measurement equipment $g(t)$. Similarly, by channel measurement the received signal can be calculated as

$$y(t) = x(t) * g(t) * h(t). \tag{2}$$

Taking Fourier transformations of (1) and (2), we can obtain the frequency domain channel transfer functions (CTFs) by direct calibration and channel measurement, which can be expressed as

$$Y_{th}(f) = X(f)G(f) \tag{3}$$

and

$$Y(f) = X(f)G(f)H(f). \tag{4}$$

Taking the inverse fast Fourier transform (IFFT) of $H(f)$, the CIR can be obtained as

$$h(t) = IFFT(H(f)) = IFFT(Y(f)/Y_{th}(f)). \tag{5}$$

*2) Estimation of Channel Parameters:* The channel parameters of the $l$th multipath components (MPCs) include complex amplitude $\alpha_l$, delay $\tau_l$, azimuth angle $\phi_l$, elevation angle $\theta_l$, and Doppler frequency $\nu_l$. Then the received signal is rewritten as

$$\begin{aligned}\boldsymbol{y}(t) = &\sum_{l=1}^{L} \alpha_l e^{j2\pi\nu_l t} c_R(\boldsymbol{\Omega}_{R,l}) c_T(\boldsymbol{\Omega}_{T,l})^T x(t-\tau_l) \\ &+ \sqrt{\frac{N_0}{2}} \boldsymbol{N}(t).\end{aligned} \tag{6}$$

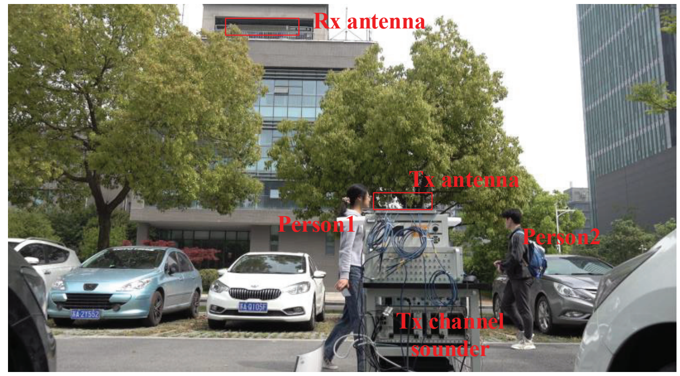


(a) The single-user channel measurement in an urban scenario.


(b) The ultra-massive MIMO antenna configuration with the ULA.


(c) The ultra-massive MIMO antenna configuration with the DULA.

Fig. 3. The (a) single-user channel measurement in an urban scenario and the ultra-massive MIMO antenna configurations with the (b) ULA and (c) DULA.


Fig. 4. Multi-user channel measurement in an urban scenario.

In (6), $(\cdot)^T$ is the transpose operator, $\boldsymbol{N}(t)$ is the standard complex white Gaussian noise with PSD $N_0$, and the response vector $c_R(\boldsymbol{\Omega}_{R,l})$ of the Rx array and the steering vector $c_T(\boldsymbol{\Omega}_{T,l})$ of the Tx array [39] can be expressed as

$$\begin{aligned}c_T(\boldsymbol{\Omega}_{T,l}) = [&e^{j2\pi\lambda^{-1}(\boldsymbol{\Omega}_{T,l}\cdot \boldsymbol{r}_{T,1})}, e^{j2\pi\lambda^{-1}(\boldsymbol{\Omega}_{T,l}\cdot \boldsymbol{r}_{T,2})}, \\ &\ldots, e^{j2\pi\lambda^{-1}(\boldsymbol{\Omega}_{T,l}\cdot \boldsymbol{r}_{T,M_T})}]^T\end{aligned} \tag{7}$$

and

$$\begin{aligned}c_R(\boldsymbol{\Omega}_{R,l}) = [&e^{j2\pi\lambda^{-1}(\boldsymbol{\Omega}_{R,l}\cdot \boldsymbol{r}_{R,1})}, e^{j2\pi\lambda^{-1}(\boldsymbol{\Omega}_{R,l}\cdot \boldsymbol{r}_{R,2})}, \\ &\ldots, e^{j2\pi\lambda^{-1}(\boldsymbol{\Omega}_{R,l}\cdot \boldsymbol{r}_{R,M_R})}]^T.\end{aligned} \tag{8}$$

Here, $M_T$ and $M_R$ represent the number of Tx antennas and Rx antennas, respectively, $\boldsymbol{r}_{T,p} (p = 1, 2, \ldots, M_T)$ represents the position vector of the $p$th antenna element of the Tx array, and $\boldsymbol{r}_{R,q}(q = 1, 2, \ldots, M_R)$ represents the position vector of the $q$th antenna element of the Rx array. The unit vectors $\mathbf{\Omega}_{T,l}$ and $\mathbf{\Omega}_{R,l}$ can be expressed as

$$\mathbf{\Omega}_{T,l} = [\sin(\theta_{T,l})\sin(\phi_{T,l}), \sin(\theta_{T,l})\cos(\phi_{T,l}), \cos(\theta_{T,l})]^T \tag{9}$$

and

$$\mathbf{\Omega}_{R,l} = [\sin(\theta_{R,l})\sin(\phi_{R,l}), \sin(\theta_{R,l})\cos(\phi_{R,l}), \cos(\theta_{R,l})]^T. \tag{10}$$

Here, $\theta_{T,l}$ is the elevation angle of departure (EAoD) of $l$th MPCs, $\phi_{T,l}$ is the azimuth angle of departure (AAoD) of $l$th MPCs, $\theta_{R,l}$ is the elevation angle of arrival (EAoA) of $l$th MPCs, and $\phi_{R,l}$ is the azimuth angle of arrival (AAoA) of $l$th MPCs. The detailed space-alternating generalized expectation-maximization (SAGE) channel parameters extraction algorithm has been investigated [40]–[42].

## III. Ultra-massive MIMO Channel Modeling

As illustrated in Fig. 5, large ULAs are deployed at the Tx and Rx sides in the proposed general channel model. For the Tx, the number of antennas is $M_T$ and the symbol of antenna elements is expressed as $A_p^T$ $(p = 1, 2, \cdots, M_T)$, and the distance of adjacent antenna elements is $\delta_T$. For the Rx, the number of the antennas is $M_R$ and the symbol of antenna element is expressed as $A_q^R$ $(q = 1, 2, \cdots, M_R)$, and the distance of adjacent antenna elements is $\delta_R$. The angle of elevation is $\beta_E^T$ and the angle of azimuth is $\beta_A^T$ at the Tx. The angle of elevation is $\beta_E^R$ and the angle of azimuth is $\beta_A^R$ at the Rx. The propagation path from the Tx to the Rx is modeled as multi-bounce model, which can be simplified to twin-cluster model [25]. The first bounce cluster is expressed as $C_n^A$ and the last bounce cluster is expressed as $C_n^Z$. A virtual link is abstracted between $C_n^A$ and $C_n^Z$. When the first bounce cluster $C_n^A$ and the last bounce cluster $C_n^Z$ completely overlap, i.e., the delay of the virtual link equals to zero, the proposed twin-cluster model can capture the single-bounce transmission. For a given scenario, the number of propagation paths from the $p$th antenna $A_p^T$ to the $q$th antenna $A_q^R$ at time $t$ can be defined as $N_{qp}(t)$ and the number of scatterers of the $n$th propagation path can be defined as $M_n(t)$. Note that the Tx, Rx, and clusters of the model have time-varying velocities and arbitrary trajectories. In addition, all the parameters defined in the proposed general channel model are time-varying. Just to be clear, Table III summarizes the definitions of the important and remaining parameters.

Wireless propagation channel fading includes large scale fading (LSF) caused by pass loss ($PL$) and the shadowing ($SH$) of fixed obstacles on the propagation path, and small scale fading (SSF) caused by the fast fluctuation of signal due to the superposition of MPCs. Note that wireless propagation channel fading has been represented in the complete channel matrix as

$$\mathbf{H} = [PL \cdot SH]^{1/2}\,\mathbf{H}_s. \tag{11}$$

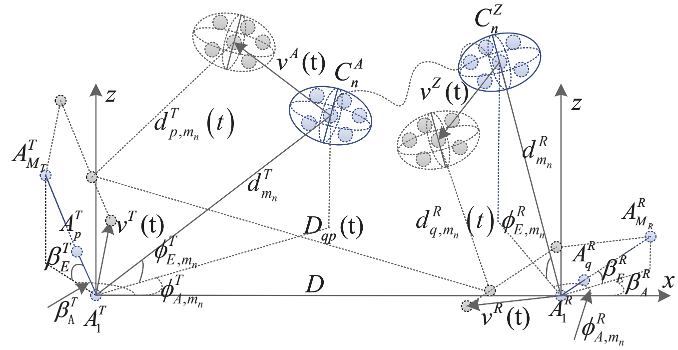


Fig. 5. A general 3D ultra-massive MIMO GBSM for 6G communication systems.

In (11), $\mathbf{H}_s$ is the matrix of SSF, which can be expressed as

$$\mathbf{H}_s = \left[h_{qp}(t,\tau)\right]_{M_R \times M_T}. \tag{12}$$

The CIR from the $p$th antenna $A_p^T$ at the Tx to the $q$th antenna $A_q^R$ at the Rx $h_{qp}(t,\tau)$ includes the LOS component and the NLOS components can be calculated as

$$h_{qp}(t,\tau) = \sqrt{\frac{K_{RF}(t)}{K_{RF}(t)+1}}h_{qp}^L(t,\tau) + \sqrt{\frac{1}{K_{RF}(t)+1}}h_{qp}^N(t,\tau). \tag{13}$$

In (13), the symbol of LOS component is expressed as $h_{qp}^L(t,\tau)$, the symbol of NLOS components is expressed as $h_{qp}^N(t,\tau)$, and the symbol of Rician K-factor is expressed as $K_{RF}(t)$. Furthermore, the LOS component $h_{qp}^L(t,\tau)$ is further calculated as

$$\begin{aligned} h_{qp}^L(t,\tau) = & \begin{bmatrix} F_{q,V_p}(\phi_{E,L}^R(t), \phi_{A,L}^R(t)) \\ F_{q,H_p}(\phi_{E,L}^R(t), \phi_{A,L}^R(t)) \end{bmatrix}^T \\ & \times \begin{bmatrix} e^{j\theta_L^{V_pV_p}} & 0 \\ 0 & -e^{j\theta_L^{H_pH_p}} \end{bmatrix} \begin{bmatrix} F_{p,V_p}(\phi_{E,L}^T(t), \phi_{A,L}^T(t)) \\ F_{p,H_p}(\phi_{E,L}^T(t), \phi_{A,L}^T(t)) \end{bmatrix} \\ & \times\ e^{j2\pi f_c \tau_{qp}^L(t)}\delta(\tau - \tau_{qp}^L(t)). \end{aligned} \tag{14}$$

The NLOS components $h_{qp}^N(t,\tau)$ is further calculated as

$$\begin{aligned} h_{qp}^N(t,\tau) = & \sum_{n=1}^{N_{qp}(t)} \sum_{m=1}^{M_n(t)} \begin{bmatrix} F_{q,V_p}(\phi_{E,m_n}^R(t), \phi_{A,m_n}^R(t)) \\ F_{q,H_p}(\phi_{E,m_n}^R(t), \phi_{A,m_n}^R(t)) \end{bmatrix}^T \\ & \times \begin{bmatrix} e^{j\theta_{m_n}^{V_pV_p}} & \sqrt{\kappa_{m_n}^{-1}(t)}e^{j\theta_{m_n}^{V_pH_p}} \\ \sqrt{\kappa_{m_n}^{-1}(t)}e^{j\theta_{m_n}^{H_pV_p}} & e^{j\theta_{m_n}^{H_pH_p}} \end{bmatrix} \\ & \times \begin{bmatrix} F_{p,V_p}(\phi_{E,m_n}^T(t), \phi_{A,m_n}^T(t)) \\ F_{p,H_p}(\phi_{E,m_n}^T(t), \phi_{A,m_n}^T(t)) \end{bmatrix} \sqrt{P_{qp,m_n}(t)} \\ & \times e^{j2\pi f_c \tau_{qp,m_n}(t)} \cdot \delta(\tau - \tau_{qp,m_n}(t)). \end{aligned} \tag{15}$$

Here, $F_{p,V_p}^T(\cdot)$ and $F_{p,H_p}^T(\cdot)$ represent the antenna radiation patterns of vertical and horizontal polarizations at the Tx, $F_{q,V_p}^R(\cdot)$ and $F_{q,H_p}^R(\cdot)$ represent the antenna radiation patterns

TABLE III
DEFINITION OF KEY CHANNEL MODEL PARAMETERS.

| Parameters | Definition |
|---|---|
| $f_c$ | Carrier frequency |
| $D$ | Distance between the Tx antenna $A_1^T$ and the Rx antenna $A_1^R$ at initial time |
| $D_{qp}(t)$ | Distance between the $p$th Tx antenna $A_p^T$ and the $q$th Rx antenna $A_q^R$ at time $t$ |
| $d_{m_n}^T$ | Distance between the Tx antenna $A_1^T$ and the $m$th scatterer of the first bounce cluster $C_n^A$ at initial time |
| $d_{m_n}^R$ | Distance between the Rx antenna $A_1^R$ and the $m$th scatterer of the last bounce cluster $C_n^Z$ at initial time |
| $d_{p,m_n}^T(t)$ | Distance between the $p$th Tx antenna $A_p^T$ and the $m$th scatterer of the first bounce cluster $C_n^A$ at time $t$ |
| $d_{q,m_n}^R(t)$ | Distance between the $q$th Rx antenna $A_q^R$ and the $m$th scatterer of the last bounce cluster $C_n^Z$ at time $t$ |
| $\beta_A^T$, $\beta_A^R$ | Azimuth angles of the Tx and Rx antenna arrays, respectively |
| $\beta_E^T$, $\beta_E^R$ | Elevation angles of the Tx and Rx antenna arrays, respectively |
| $\delta_T$, $\delta_R$ | Distances of adjacent antenna elements of the Tx and Rx antenna arrays, respectively |
| $v^T(t)$, $v^R(t)$, $v^{A_n}(t)$, $v^{Z_n}(t)$ | Velocities of the Tx, Rx, first bounce cluster $C_n^A$, and last bounce cluster $C_n^Z$ at time $t$, respectively |
| $\alpha_A^T(t)$, $\alpha_A^R(t)$, $\alpha_A^{A_n}(t)$, $\alpha_A^{Z_n}(t)$ | Azimuth angles of moving direction of the Tx, Rx, first bounce cluster $C_n^A$, and last bounce cluster $C_n^Z$ at time $t$, respectively |
| $\alpha_E^T(t)$, $\alpha_E^R(t)$, $\alpha_E^{A_n}(t)$, $\alpha_E^{Z_n}(t)$ | Elevation angles of moving direction of the Tx, Rx, first bounce cluster $C_n^A$, and last bounce cluster $C_n^Z$ at time $t$, respectively |
| $\phi_{A,L}^T$, $\phi_{E,L}^T$ | AAoD and EAoD from the Tx antenna $A_1^T$ to the Rx antenna $A_1^R$ at initial time, respectively |
| $\phi_{A,L}^R$, $\phi_{E,L}^R$ | AAoA and EAoA from the Rx antenna $A_1^R$ to the Tx antenna $A_1^T$ at initial time, respectively |
| $\phi_{A,m_n}^T$, $\phi_{E,m_n}^T$ | AAoD and EAoD from the Tx antenna $A_1^T$ to the $m$th scatterer of the first bounce cluster $C_n^A$ at initial time, respectively |
| $\phi_{A,m_n}^R$, $\phi_{E,m_n}^R$ | AAoA and EAoA from the Rx antenna $A_1^R$ to the $m$th scatterer of the last bounce cluster $C_n^Z$ at initial time, respectively |
| $P_{qp,m_n}(t)$ | Power of the ray from the $p$th Tx antenna $A_p^T$ to the $q$th Rx antenna $A_q^R$ at time $t$, through the $m$th scatterer located in the first bounce cluster $C_n^A$ and the $m$th scatterer located in the last bounce cluster $C_n^Z$ |

of vertical and horizontal polarizations at the Rx, respectively, $\theta_L^{V_pV_p}$ and $\theta_L^{H_pH_p}$ represent the random phases of vertical and horizontal polarizations of LOS component which are uniformly distributed in $[0, 2\pi)$, $\theta_{m_n}^{V_pV_p}$, $\theta_{m_n}^{H_pH_p}$, and $\theta_{m_n}^{V_pH_p}$ ($\theta_{m_n}^{H_pV_p}$) represent the random phases of vertical, horizontal, and crossed polarizations of NLOS components which are uniformly distributed in $[0, 2\pi)$, $\kappa_{m_n}$ represents the cross polarization ratio, $P_{qp,m_n}(t)$ represents the power of the ray from the $p$th antenna $A_p^T$ to the $q$th antenna $A_q^R$ at time $t$, through the $m$th scatterer located in the first bounce cluster $C_n^A$ and the $m$th scatterer located in the last bounce cluster $C_n^Z$, and $\tau_{qp,m_n}(t)$ represents the delay of the ray from the $p$th antenna $A_p^T$ to the $q$th antenna $A_q^R$ at time $t$, through the $m$th scatterer located in the first bounce cluster $C_n^A$ and the $m$th scatterer located in the last bounce cluster $C_n^Z$, which can be calculated as

$$\tau_{qp,m_n}(t) = \frac{d_{qp,m_n}(t)}{c}. \tag{16}$$

In (16), $c$ is the speed of light, $d_{qp,m_n}(t)$ is the distance between the $p$th antenna $A_p^T$ at the Tx and the $q$th antenna $A_q^R$ at the Rx at time $t$, through the $m$th scatterer located in the first bounce cluster $C_n^A$ and the $m$th scatterer located in the last bounce cluster $C_n^Z$, which is calculated as

$$d_{qp,m_n}(t) = \parallel \vec{d}_{p,m_n}(t) \parallel + \parallel \vec{d}_{q,m_n}(t) \parallel + \tilde{\tau}_{m_n} c. \tag{17}$$

Here, $\parallel \cdot \parallel$ represents the two norm operator, $\tilde{\tau}_{m_n}$ is the virtual link delay from the scatterer located in first bounce cluster to the scatterer located in last bounce cluster. Due to the reciprocity between the uplink channel and downlink channel, the calculations of $\vec{d}_{p,m_n}(t)$ and $\vec{d}_{q,m_n}(t)$ are the same. Let us take $\vec{d}_{p,m_n}(t)$ as an example, which is calculated as

$$\vec{d}_{p,m_n}(t) = \vec{d}_{m_n} + \int_0^t \vec{v}^{A_n}(t)dt - \int_0^t \vec{v}^T(t)dt - \vec{l}_p^T. \tag{18}$$

In (18), $\vec{d}_{m_n}$ is the distance vector from the first antenna $A_1^T$ at the Tx to the $m$th scatterer located in the first bounce cluster $C_n^A$ at initial time, $\vec{l}_p^T$ is the distance vector from the first antenna $A_1^T$ to the $p$th antenna $A_p^T$ at the Tx.

The non-normalized power of the ray $P_{qp,m_n}(t)$ can be expressed as

$$P'_{qp,m_n}(t) = \exp\left(-\tau_{qp,m_n}(t)\frac{r_\tau - 1}{r_\tau DS}\right)10^{\frac{-Z_{qp,m_n}}{10}}. \tag{19}$$

In (19), $r_\tau$ is the delay distribution proportionality factor and $Z_{qp,m_n}$ is the per ray shadowing [43]. The normalized power of the ray can be expressed as [27]

$$P_{qp,m_n}(t) = \frac{P'_{qp,m_n}(t)}{\sum_{n=1}^{N_{qp}(t)} \sum_{m=1}^{M_n(t)} P'_{qp,m_n}(t)}. \tag{20}$$

The movement of the Tx causing the change of positions, the large scale parameters (LSPs) as well as corresponding small scale parameters (SSPs) should be updated. Ultra-massive MIMO channel modeling includes two parts. One is initialization and the other is update. First, we should define simulation parameters, network layout, and scenario. Then, the Tx trajectory should be defined and initial LSPs should be generated. Next, the initial SSPs should be generated according to the LSPs. Finally, we should update the LSPs as well as the SSPs to get channel coefficient. We will introduce the generations of LSPs and SSPs, and the cluster evolution process in details.

### A. The Generation of LSPs with Spatial Consistency

The LSPs refer to DS, angle spreads (ASs), $K_{RF}$, $SH$, and cross polarization ratio $\kappa$, which depend on the position of the Tx and the position of the Rx. The AS includes azimuth spread and elevation spread, which can be further expressed as azimuth spread of departure (ASD), azimuth spread of arrival (ASA), elevation spread of departure (ESD), and elevation spread of arrival (ESA). The detailed sum-of-sinusoids (SoS) method that used for generating LSPs is recommended in QuaDRiGa [44]. Because the generation of LSPs is related to the spatial positions, the proposed model inherently has spatial consistency property.

### B. The Generation of SSPs

The SSPs are generated according to LSPs. The cluster delays, powers, and angles can be obtained according to 3GPP TR 38.901 in [43]. The distances between the Tx or Rx to the corresponding clusters are modeled as random variables generated with an exponential distribution. Assuming that the center of a cluster is the origin. The distribution of positions $(x', y', z')$ of scatterers in the cluster is modeled as ellipsoid Gaussian scattering distribution [27], which is calculated as

$$p(x', y', z') = \frac{\exp(-\frac{x'^2}{2\sigma_{DS}^2} - \frac{y'^2}{2\sigma_{AS}^2} - \frac{z'^2}{2\sigma_{ES}^2})}{(2\pi)^{3/2}\sigma_{DS}\sigma_{AS}\sigma_{ES}}. \tag{21}$$

In (21), $\sigma_{AS}$ and $\sigma_{ES}$ are the standard derivations for the scatterers' azimuth angles and elevation angles distributions in one cluster, respectively, and $\sigma_{DS}$ is the standard derivation which describes the distribution of the delays from the Tx or Rx to the scatterers in one cluster. Note that the $\sigma_{AS}$ and $\sigma_{ES}$ can be further expressed as $\sigma_{ASD}$ and $\sigma_{ESD}$ at the Tx, and can be further expressed as $\sigma_{ASA}$ and $\sigma_{ESA}$ at the Rx. In addition, the expression of (21) describes the locations of scatterers in the space without showing angle information. To show the angle information, we define $(\overline{d}, \overline{\phi}_E, \overline{\phi}_A)$ as the center position of one cluster [27], [45]. Then the relationship between the scatterers' positions $(x, y, z)$ in one cluster whose center position is $(\overline{d}, \overline{\phi}_E, \overline{\phi}_A)$ and the scatterers' positions $(x', y', z')$ in one cluster whose center position is the origin can be calculated as

$$\begin{bmatrix} x \\ y \\ z \end{bmatrix} = \begin{bmatrix} \cos(\overline{\phi}_{\mathrm{A}}) & -\sin(\overline{\phi}_{\mathrm{A}}) & 0 \\ \sin(\overline{\phi}_{\mathrm{A}}) & \cos(\overline{\phi}_{\mathrm{A}}) & 0 \\ 0 & 0 & 1 \end{bmatrix} \times \begin{bmatrix} \cos(\overline{\phi}_E) & 0 & \sin(\overline{\phi}_E) \\ 0 & 1 & 0 \\ -\sin(\overline{\phi}_E) & 0 & \cos(\overline{\phi}_E) \end{bmatrix} \begin{bmatrix} x' - d \\ y' \\ z' \end{bmatrix}. \tag{22}$$

Substituting $x = d\cos(\phi_{\mathrm{E}})\cos(\phi_{\mathrm{A}})$, $y = d\cos(\phi_{\mathrm{E}})\sin(\phi_{\mathrm{A}})$, and $z = d\sin(\phi_{\mathrm{E}})$ into (22), the azimuth angles of scatterers, the elevation angles of scatterers, and the distances between the Tx or Rx and the scatterers located in one cluster can be obtained in the spherical coordinate system.

### C. The Evolution Process of the Clusters

The proposed channel model can support the characteristic of STF non-stationarity. For ultra-massive MIMO antenna array, we can observe the phenomenon that along the array clusters may appear and disappear. In addition, clusters will go through a birth-death process with the movement of the Tx along the time axis [46]. Note that the evolution process of the cluster in the space domain and time domain of the proposed general channel model is modeled jointly. For the Tx, the symbol of initial time is expressed as $t_i$ and the symbol of antenna element is expressed as $A_p^T$, and the symbol of the cluster is expressed as $C_p^T(t_i)$. For the Rx, the symbol of initial time is expressed as $t_i$ and the symbol of antenna element is expressed as $A_q^R$, and the symbol of the cluster is expressed as $C_q^R(t_i)$. At the next time $t_i + \triangle t$, the clusters will evolve into $C_{p+1}^T(t_i + \triangle t)$ at the Tx and $C_{q+1}^R(t_i + \triangle t)$ at the Rx. The evolution process of the clusters in the space domain and time domain can be expressed as

$$C_p^T(t_i) \xrightarrow{E} C_{p+1}^T(t_i + \triangle t) \quad (p = 1, 2, \cdots, M_T - 1) \tag{23}$$

and

$$C_q^R(t_i) \xrightarrow{E} C_{q+1}^R(t_i + \triangle t) \quad (q = 1, 2, \cdots, M_R - 1). \tag{24}$$

In (23) and (24), $\xrightarrow{E}$ is the symbol of the evolution process of clusters. By the evolution process of the clusters in the space domain and time domain, we can obtain the probabilities of the survival clusters at the Tx and Rx sides expressed as

$$P_{\text{sur}}^T(\triangle t, \delta_p) = e^{-\lambda^R\left[(\epsilon_1^T)^2 + (\epsilon_2^T)^2 + 2\epsilon_1^T\epsilon_2^T\cos(\alpha_A^T - \beta_A^T)\right]^{1/2}} \tag{25}$$

and

$$P_{\text{sur}}^R(\triangle t, \delta_q) = e^{-\lambda^R\left[(\epsilon_1^R)^2 + (\epsilon_2^R)^2 + 2\epsilon_1^R\epsilon_2^R\cos(\alpha_A^R - \beta_A^R)\right]^{1/2}}. \tag{26}$$

Here, $\lambda^R$ is the recombination rate of the cluster, $\epsilon_1^T = \frac{\delta_p \cos\beta_E^T}{D_c^A}$ $(\delta_p = (p-1)\delta_T)$ and $\epsilon_2^T = \frac{v_T \triangle t}{D_c^S}$ represent the distance differences due to the array evolution and time evolution at the Tx, respectively, $\epsilon_1^R = \frac{\delta_q \cos\beta_E^R}{D_c^A}$ $(\delta_q = (q-1)\delta_R)$ and $\epsilon_2^R = \frac{v_R \triangle t}{D_c^S}$ represent the distance differences due to the array evolution and the time evolution at the Rx, respectively, $D_c^A$ is the coefficient in the space domain determined by the scenario, and $D_c^S$ is coefficient in the time domain determined by the scenario. Combined with cluster evolution in the frequency domain, the survival probability considering cluster evolution in STF domains can be obtained as

$$P_{\text{sur}}(\triangle t, \delta_p, \delta_q, \triangle f) = P_{\text{sur}}^T(\triangle t, \delta_p) \cdot P_{\text{sur}}^R(\triangle t, \delta_q) \cdot P_{\text{sur}}(\triangle f). \tag{27}$$

The probability of the survival clusters in the frequency domain $P_{\text{sur}}(\triangle f)$ is calculated as [47]

$$P_{\text{sur}}(\triangle f) = e^{-\lambda^R \frac{F(\triangle f)}{D_c^f}}. \tag{28}$$

In (28), $F(\triangle f)$ and $D_c^f$ can be obtained by channel measurements. Finally, the mean value of the newly generated cluster considering STF evolution process is calculated as

$$E\left[N_{\text{new}}\right] = \frac{\lambda^G}{\lambda^R}(1 - P_{\text{sur}}(\triangle t, \delta_p, \delta_q, \triangle f)) \tag{29}$$

where $\lambda^G$ is the generation rate of the cluster.

For mmWave and terahertz (THz) communications with large bandwidth, clusters will go through a birth-death process in different subcarrier frequencies and frequency non-stationarity needs to be considered. For sub-6 GHz bands, the proposed general channel model can be simplified to a frequency-stationary channel model by setting $P_{\text{sur}}(\triangle f) = 1$.

### D. Update of the Parameters

Due to the movement of the Tx, the LSPs need to be updated. When the position of the Tx and the position of the Rx are determined, the corresponding LSPs can be generated. The SSPs can be updated according to LSPs. Furthermore, the elevation angles, azimuth angles, and the distances from the centers of clusters to the Tx or Rx for the new clusters as well as the parameters of scatterers need to be updated.

### E. The Generality of the Channel Model

It is worth mentioning that the proposed channel model is suitable for mmWave communications with distinguishable ray delay, V2V communications with the time-varying speeds for the Tx and Rx [48]–[51], 3D communication environments with azimuth and elevation dimensions, HST communications with high speed of the Tx or Rx, etc. By adjusting the corresponding parameters, we can easily apply the proposed general channel model to different frequency bands and communication scenarios.

## IV. Channel Measurements and Simulation Results and Analysis

In this section, channel measurements and simulation results are presented. Some simulation parameters of the model related to system configuration were set according to ultra-massive MIMO channel measurements, such as carrier frequency, antenna configuration, antenna height, positions of the Tx and Rx, etc. Some model parameters were extracted by measurement data processing results, such as DS, ASA, etc. Some model parameters were determined by fitting statistical properties to the corresponding channel measurement data, such as the generation rate of the cluster $\lambda^G$, the recombination rate of the cluster $\lambda^R$, the standard derivations of the scatterers' azimuth angle distributions $\sigma_{ASA}$ and $\sigma_{ASD}$, the standard derivations of the scatterers' elevation angle distributions $\sigma_{ESA}$ and $\sigma_{ESD}$, the standard derivations of the scatterers' delays from the Tx or Rx to the scatterers distribution $\sigma_{DS}$, etc. The rest model parameters were randomly generated according to the 3GPP TR 38.901 channel model.

### A. Non-Stationarity and Spatial Consistency

*1) Delay PSD:* Fig. 6 shows the single-user channel measurement delay PSD with the Tx moving along Route 1. There are 2400 snapshots lasting about 27.6 s. As we can see from Fig. 6, the variation of the LOS component is significant, which verifies the temporal non-stationarity of the channel [52]. Spatial consistency refers to the strong correlation of channel parameters between different locations, when they are close to each other. The continuous and slow variations of the delay PSD with Tx positions shown as snapshots clearly demonstrates the spatial consistency. Figs. 7 (a) and (b) present the single-user measured delay PSD and estimated delay PSD from SAGE with ULA and DULA at the Rx side, respectively. It should be known that in SAGE algorithm, 100 MPCs are selected to extract channel parameters by weighing algorithm accuracy and complexity. We can conclude that most MPCs can be estimated and the estimated delay PSD is consistent with the measured delay PSD, which verifies the accuracy of SAGE algorithm.

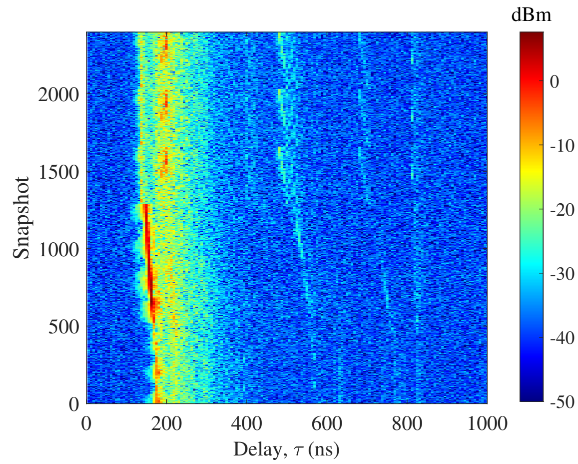


Fig. 6. An illustration of the measured delay PSD along Route 1.

*2) RMS DS:* The RMS DS describes the power of MPCs spreading over the delay. The reciprocal of the RMS DS represents the coherence bandwidth. Further, the RMS DS can be expressed as [40]

$$\text{DS} = \sqrt{\frac{\sum_{l=1}^{L} P_l \tau_l^2}{\sum_{l=1}^{L} P_l} - \left( \frac{\sum_{l=1}^{L} P_l \tau_l}{\sum_{l=1}^{L} P_l} \right)^2} \tag{30}$$

where $P_l$ is the power of the $l$th MPCs, and can be expressed as $P_l = |\alpha_l|^2$.

Fig. 8 shows the cumulative distribution functions (CDFs) of $\log_{10}(\text{DS}/1\ \text{s})$ in LOS and NLOS environments, which can be fitted by base 10 lognormal distributions with $N(-7.55, 0.18^2)$ and $N(-7.41, 0.15^2)$, respectively. The base 10 lognormal distribution refers to that the CDF of DS is obtained by the operation of $\log_{10}(\text{DS}/1\ \text{s})$. The relationship between the coherence bandwidth $B_c$ and RMS DS is $B_c \approx \frac{1}{\text{DS}}$. Taking the reciprocal of the RMS DS, the coherence bandwidths can be obtained with 35.5 MHz and 25.7 MHz in LOS and NLOS environments, respectively. The mean value of DS in LOS environments is smaller than that in NLOS environments while the variance in LOS environments is larger than that in NLOS environments. In addition, the simulation results of the proposed general channel model are consistent with the measurement results, which indicates that the model is highly accurate.

*3) RMS AS:* The RMS AS represents the power of MPCs spreading over the angle. The reciprocal of the RMS AS is the coherence distance. Note that the RMS AS includes the RMS

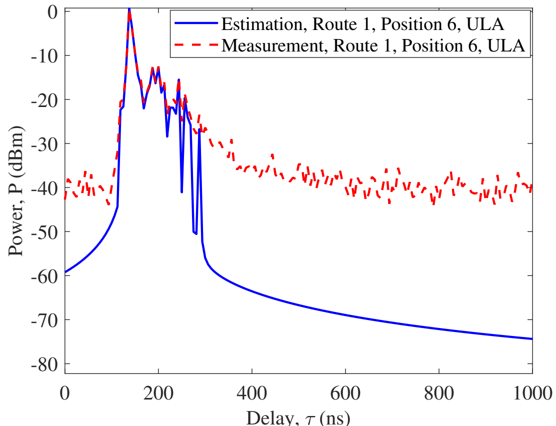


(a) The measured and estimated delay PSDs for the ULA.

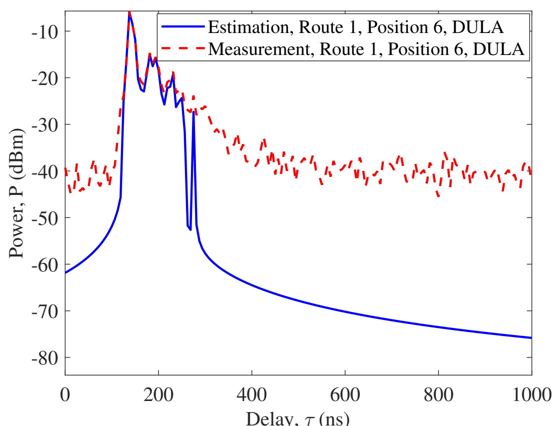


(b) The measured and estimated delay PSDs for the DULA.

Fig. 7. The measured and estimated delay PSDs of the single user in a LOS environment.

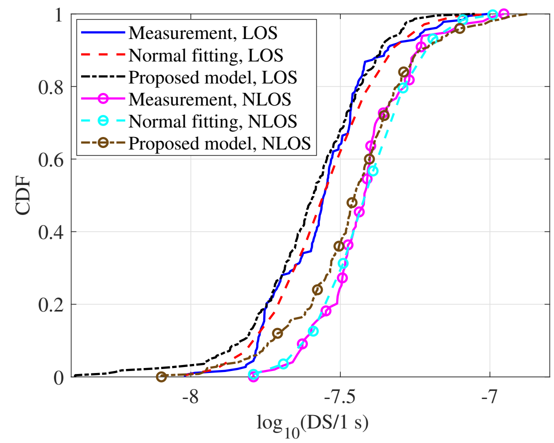


Fig. 8. CDFs of $\log_{10}(\text{DS}/1\ \text{s})$ in LOS and NLOS environments (LOS: $\sigma_{ASA}$ = 7 m, $\sigma_{ASD}$ = 7 m, $\sigma_{ESA}$ = 5 m, $\sigma_{ESD}$ = 5 m, $\sigma_{DS}$ = 6 m, $\lambda^G$ = 20/m, $\lambda^R$ = 1/m; NLOS: $\sigma_{ASA}$ = 14 m, $\sigma_{ASD}$ = 14 m, $\sigma_{ESA}$ = 12 m, $\sigma_{ESD}$ = 12 m, $\sigma_{DS}$ = 8 m, $\lambda^G$ = 20/m, $\lambda^R$ = 1/m).

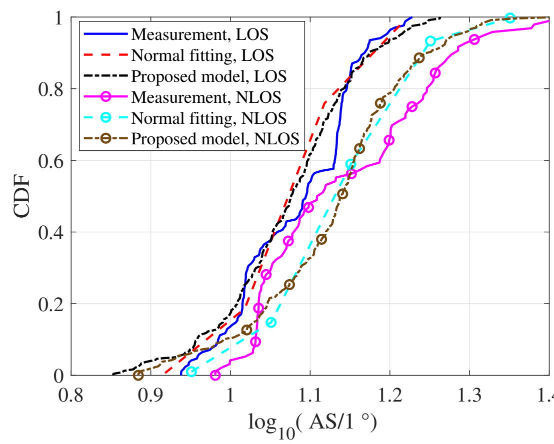


Fig. 9. CDFs of $\log_{10}(\text{AS}/1°)$ in LOS and NLOS environments (LOS: $\sigma_{ASA}$ = 7 m, $\sigma_{ASD}$ = 7 m, $\sigma_{ESA}$ = 5 m, $\sigma_{ESD}$ = 5 m, $\sigma_{DS}$ = 6 m, $\lambda^G$ = 20/m, $\lambda^R$ = 1/m; NLOS: $\sigma_{ASA}$ = 14 m, $\sigma_{ASD}$ = 14 m, $\sigma_{ESA}$ = 12 m, $\sigma_{ESD}$ = 12 m, $\sigma_{DS}$ = 8 m, $\lambda^G$ = 20/m, $\lambda^R$ = 1/m).

ASA, RMS ASD, RMS ESA, and RMS ESD, we will focus on the RMS ASA. Correspondingly, the RMS AS of ASA can be expressed as [40]

$$\text{AS} = \sqrt{\frac{\sum_{l=1}^{L} P_l \phi_{R,l}^2}{\sum_{l=1}^{L} P_l} - \left(\frac{\sum_{l=1}^{L} P_l \phi_{R,l}}{\sum_{l=1}^{L} P_l}\right)^2}. \quad (31)$$

As illustrated in Fig. 9, the CDFs of $\log_{10}(\text{AS}/1°)$ are fitted by base 10 lognormal distributions with $N(1.11, 0.10^2)$ in LOS environments and $N(1.13, 0.09^2)$ in NLOS environments, respectively. The base 10 lognormal distribution refers to that the CDF of AS is obtained by the operation of $\log_{10}(\text{AS}/1°)$. The relationship between the coherence distance $D_c$ and RMS AS is $D_c \approx \frac{180\lambda}{\pi \text{AS}}$. Taking the reciprocal of the RMS AS, the coherence distances can be obtained with 0.25 m and 0.24 m, which are about 7.4 and 7.1 antennas spacing in LOS and NLOS environments, respectively. Compared with NLOS environments, the mean value of AS is smaller while the variance is larger in LOS environments, which is consistent with the fact that there are more scattering components in NLOS environments than those in LOS environments. The consistency of simulation results and measurement results of AS validates the accuracy of the proposed general channel model.

*4) SCCF:* The SCCF describes the correlation of different antennas along the array, which can be expressed as

$$\begin{aligned}\rho_{qp,q'p'}(t;\delta_T,\delta_R) &= E\left[h_{qp}(t)h^*_{q'p'}(t)\right] \\ &= \frac{K_{RF}(t)}{K_{RF}(t)+1}\cdot\rho^L_{qp,q'p'}(t;\delta_T,\delta_R) \\ &+ \frac{1}{K_{RF}(t)+1}\cdot\rho^N_{qp,q'p'}(t;\delta_T,\delta_R). \quad (32)\end{aligned}$$

Here, $p$ and $p'$ represent the different Tx antenna indices, $q$ and $q'$ represent the different Rx antenna indices, $E[\cdot]$ represents the operator of expectation, and $(\cdot)^*$ represents the conjugate operator.

As illustrated in Fig. 10, the distance between the antennas has obvious effect on the SCCF and large distance leads to a decrease in the SCCF. Furthermore, the consistency of the measured and simulated single-user SCCFs verifies that the proposed general channel model is applicable to the measurement scenario. Taking 0.5 as the threshold [53], the

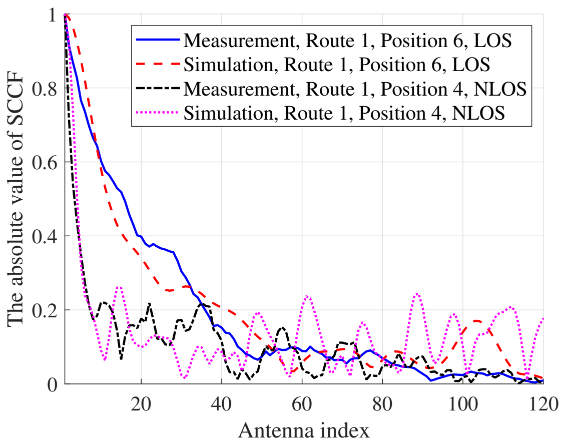


Fig. 10. The measured and simulated single-user SCCFs for the ULA in a LOS environment and a NLOS environment (LOS: $\sigma_{ASA}$ = 5 m, $\sigma_{ASD}$ = 5 m, $\sigma_{ESA}$ = 5 m, $\sigma_{ESD}$ = 5 m, $\sigma_{DS}$ = 4 m, $\lambda^G$ = 20/m, $\lambda^R$ = 1/m; NLOS: $\sigma_{ASA}$ = 15 m, $\sigma_{ASD}$ = 15 m, $\sigma_{ESA}$ = 15 m, $\sigma_{ESD}$ = 15 m, $\sigma_{DS}$ = 7 m, $\lambda^G$ = 20/m, $\lambda^R$ = 1/m).

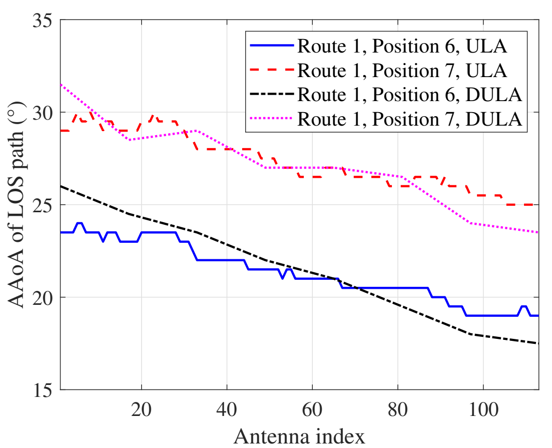


Fig. 11. The AAoAs of LOS path of the single user in a LOS environment.

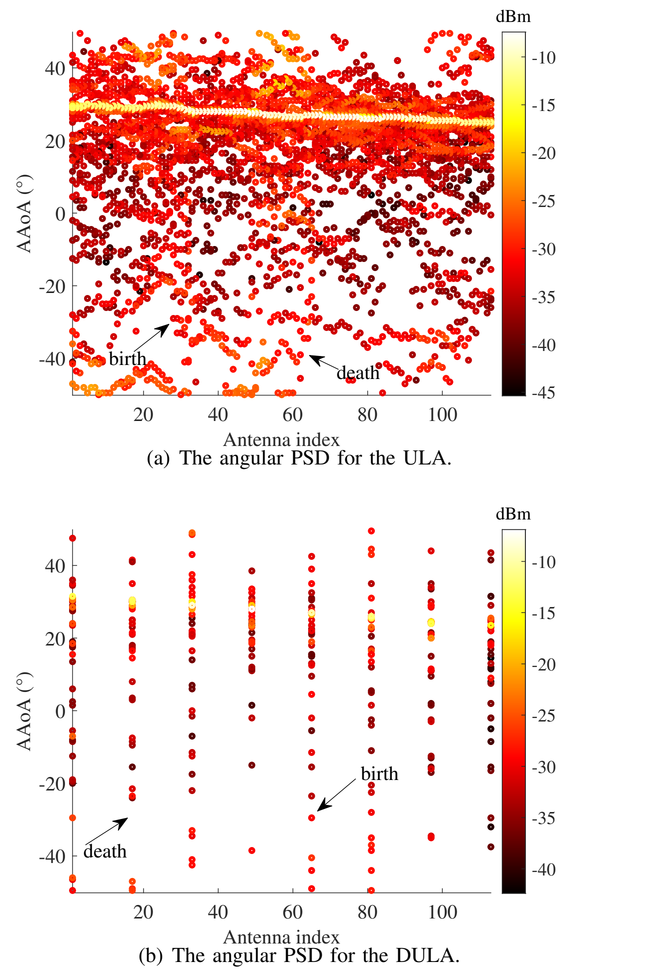


Fig. 12. The angular PSD of the single user in a LOS environment (Route 1, Position 7).

coherence distance of 0.50 m can be obtained in a LOS environment. Note that the coherence distance of 0.50 m is about 14.8 antennas spacing. Taking 0.5 as the threshold, the coherence distance of 0.10 m can be obtained in a NLOS environment. Similarly, the coherence distance of 0.10 m is about 2.9 antennas spacing. The conclusion that the coherence distance is larger in LOS environments than that in NLOS environments can be obtained.

### B. Spherical Wavefront Property

*1) AAoA of LOS path:* As illustrated in Fig. 11, the AAoAs of LOS path gradually drift along the array. We can observe that for the DULA the range of variation for angle is larger than that for the ULA, which indicates that the longer array for ultra-massive MIMO will make the spherical wavefront property more obvious.

*2) Angular PSD:* Figs. 12 (a) and (b) show the angular PSD for ULA and DULA in a LOS environment, respectively. Similarly, we can find that the AAoAs of LOS path drift along the array. In addition, the birth and death of MPCs along array axis show the spatial non-stationarity of ultra-massive MIMO antenna array.

### C. Channel Hardening Property

*1) Normalized User-side Correlation Matrix:* The normalized user-side correlation matrix describes the correlation between users, which can be calculated as

$$\boldsymbol{C}_{\text{user}} = \frac{1}{N_s N_f} \sum_{s,f} \frac{|\mathbf{H}^T(s,f)\mathbf{H}^*(s,f)|}{\| \mathbf{H}^T(s,f) \| \| \mathbf{H}^*(s,f) \|}. \tag{33}$$

Here, $N_s$ is the number of snapshots, $N_f$ is the number of frequency points, $\mathbf{H}(s,f)$ is the $M_R \times KM_T$ channel matrix for the $s$th snapshot and $f$th frequency point, $K$ and $M_T$ indicate that there are $K$ users and $M_T$ antennas for each user, respectively, and $M_R$ indicates that there are $M_R$ BS antennas.

The normalized correlation matrices of 4 users with the distance between users $D_{\text{user}}$ = 0.2 m when the Rx antenna array equipped with the ULA and DULA are illustrated in Figs. 13 (a) and (b), respectively. Note that the dimension of the normalized user-side correlation matrix in Fig. 13 is actually 16×16 and the dimension of the normalized user-side correlation matrix between two users is 4×4. Therefore, the

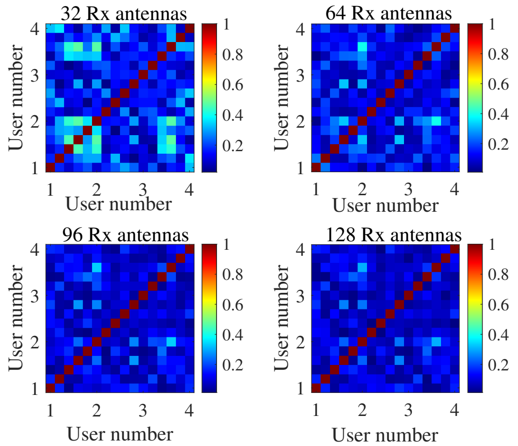


(a) The normalized user-side correlation matrix with different Rx antenna numbers for the ULA.

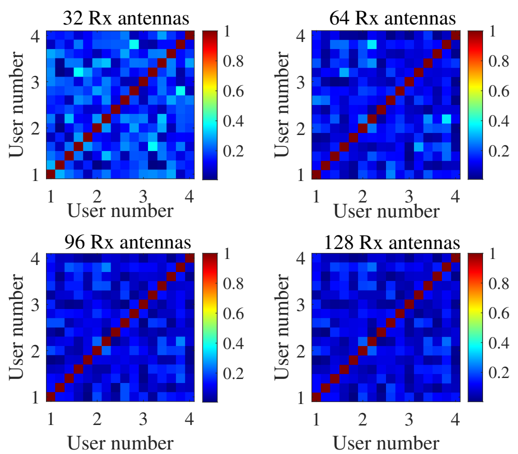


(b) The normalized user-side correlation matrix with different Rx antenna numbers for the DULA.

Fig. 13. The normalized user-side correlation matrix with different Rx antenna numbers in a LOS environment (Route 1, Position 7, $D_{\text{user}}$ = 0.2 m).

non-integer values in Fig. 13 represent the correlation between different antennas belonging to corresponding users. The ULA has larger correlation compared with the DULA specially in the case that 32 and 64 BS antennas are used. The correlation between users will decrease when we increase the number of BS antennas. As the number of BS antennas increases from 32 to 128, the value of the non-diagonal element of the correlation matrix gradually decreases when taking value 1 of the diagonal element as a reference.

*2) SVS:* The SVS of the channel matrix is an indicator to evaluate the joint orthogonality of users [18], [54]. Singular values are generated by singular value decomposition (SVD) of the channel matrix. The SVD is an efficient way to decompose an ultra-massive MIMO channel into multiple parallel single-input single-output (SISO) channels [54]. The SVD of the transpose of the channel matrix can be calculated as

$$\mathbf{H}^T = \mathbf{U}_T \mathbf{\Sigma} \mathbf{U}_R. \tag{34}$$

In (34), $\mathbf{U}_T$ is a $KM_T \times KM_T$ unitary matrix, $\mathbf{U}_R$ is an $M_R \times M_R$ unitary matrix, and $\mathbf{\Sigma}$ is a $KM_T \times M_R$ diagonal matrix composed of singular values, which are also the non-negative square roots of the eigenvalues of the matrix $\mathbf{H}^T\mathbf{H}^*$ [55]. In general, $KM_T$ is smaller than $M_R$. For example, in our channel measurements, $KM_T = 16$ is much smaller than $M_R = 128$. Thus, the number of singular values is $KM_T$.

The SVS can be expressed as

$$\kappa_{\text{svs}} = \frac{\max\limits_j \sigma_j}{\min\limits_j \sigma_j} \in [1, +\infty) \tag{35}$$

where $\sigma_1, \sigma_2, \cdots, \sigma_{KM_T}$ are the $KM_T$ singular values. The $KM_T$ singular values represent square roots of signal powers of $KM_T$ parallel SISO channels. When the SVS is close to one, the channel vectors of different users are approximately orthogonal and the channel matrix is almost full-rank. In this case, the favorable propagation condition is satisfied. When the SVS tends to infinity, the channel matrix becomes rank-deficient and the number of parallel SISO channels is smaller than $KM_T$ [56]. Thus, the channel vectors of at least two users are non-orthogonal. Therefore, a larger SVS represents that at least two users' channel vectors are almost parallel, which means that the two users have a strong correlation.

In Fig. 14, SVSs of 4 users with the distance between users $D_{\text{user}}$ = 0.2 m when the Rx antenna array equipped with the ULA and DULA are compared. The measurement results of the ULA and DULA are in dashed and solid lines, respectively. We can see that the ULA has larger SVSs in comparison with the DULA in a LOS environment. In the case that more BS antennas make the value of SVS smaller. Larger number of BS antenna elements and longer BS antenna array will make the value of SVS smaller in LOS environments, which are the effective ways to reduce the correlation between users.

### *D. Sparse Property*

*1) DoF:* The DoF is an indicator of sparse property, which can be defined by the coupling matrix $\mathbf{\Omega}_v$ of non-vanishing power [57]–[59]

$$D = \left|\left\{(q,p) : \mathbf{\Omega}_v(q,p) \geqslant c_{\text{thresh}} \max(\Omega_v)\right\}\right|. \tag{36}$$

In (36), $\mathbf{\Omega}_v = E_{\mathbf{H}}\left[\left(\mathbf{U}_R^H \mathbf{H} \mathbf{U}_T^*\right) \odot \left(\mathbf{U}_R^T \mathbf{H}^* \mathbf{U}_T\right)\right]$, $(\cdot)^H$ represents the conjugate transpose operator, $\odot$ represents the Schur-Hadamard multiplication based on elements, and $c_{\text{thresh}}$ is the threshold which can be determined by the measurements. Here, 0.01 for $c_{\text{thresh}}$ is selected for the measurement results and analysis. Note that the upper bound value of DoF is $M_R \cdot M_T$.

*2) Diversity Level:* The diversity level is an indicator of sparse property, which is defined as [57]–[60]

$$\Psi(\mathbf{R_H}) = \left(\frac{\text{tr}(\mathbf{R_H})}{\| \mathbf{R_H} \|_{\text{F}}}\right)^2. \tag{37}$$

In (37), $\text{tr}(\cdot)$ and $\|\cdot\|_{\text{F}}$ represent the trace and Frobenius norm of the matrix, respectively, $\mathbf{R_H}$ is the full correlation matrix and can be expressed as $\mathbf{R_H} \triangleq E_{\mathbf{H}}\left[\text{vec}(\mathbf{H})\text{vec}(\mathbf{H})^H\right]$, $\text{vec}(\cdot)$ represents the operator of stacking the columns of a matrix

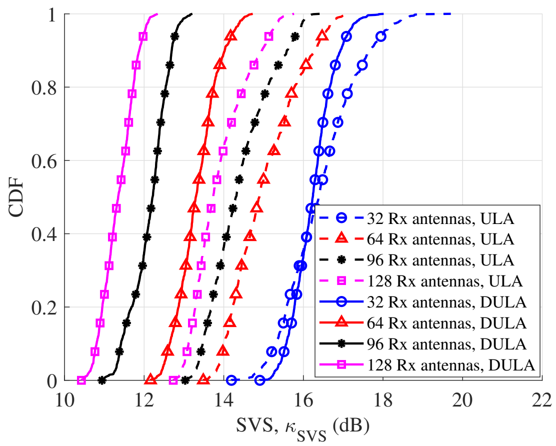


Fig. 14. The CDFs of SVSs with different Rx antenna numbers and antenna configurations in a LOS environment (Route 1, Position 7, $D_{\mathrm{user}}$ = 0.2 m).

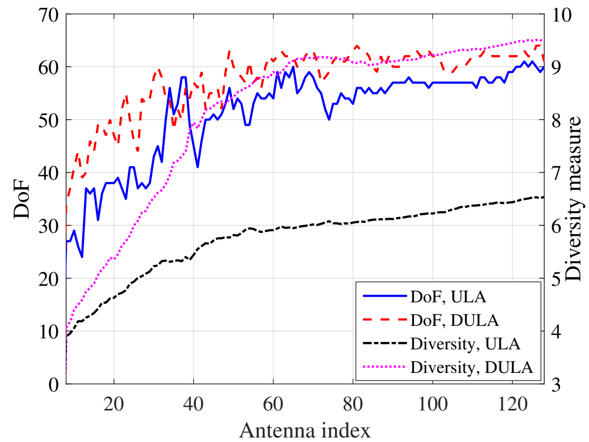


Fig. 15. The DoFs and diversity measures of the single user with different Rx antenna numbers and antenna configurations in a LOS environment (Route 1, Position 7).

into a vector. Similarly, the upper bound value of diversity level is $M_R \cdot M_T$.

Fig. 15 illustrates the DoFs and diversity measures of the single user with Rx antenna number from 8 to 128 for the ULA and DULA. We can see that the DULA has larger DoFs and diversity in comparison with the ULA under the condition of the same number of Rx antennas in a LOS environment. More BS antennas make the values of the DoFs and diversity larger. Larger number of BS antenna elements and longer BS antenna array will contribute to increase the values of DoFs and diversity in LOS environments. In addition, the values of DoFs and diversity are much smaller than the upper bound value $M_R \cdot M_T = 128 \times 8$, which clearly indicates the sparse property.

### E. Channel Capacity

Ergodic channel capacity is also called average channel capacity, which is defined as the ensemble average of the instantaneous capacities over all possible channel realizations. The single-user received power for the $s$th snapshot and $f$th frequency point is calculated as $P_r(s,f) = \| \mathbf{H}(s,f) \|^2 / M_R M_T$ and $\mathbf{H}(s,f)$ is the $M_R \times K M_T$ channel matrix for the $s$th snapshot and $f$th frequency point with $K = 1$. The single-user ergodic channel capacity is calculated as [61]

$$C = \frac{1}{N_s N_f} \sum_{s,f} \log_2 \left[ \det \left( \mathbf{I}_{M_R} + \frac{\rho}{M_T} \hat{\mathbf{H}}(s,f) \hat{\mathbf{H}}^H(s,f) \right) \right]. \tag{38}$$

In (38), $\det[\cdot]$ represents the determinant operator, $\rho$ represents the signal-to-noise ratio (SNR), $\mathbf{I}_{M_R}$ represents the identity matrix of order $M_R$, and $\hat{\mathbf{H}}(s,f)$ is the normalized channel matrix for the $s$th snapshot and $f$th frequency point which can be calculated as $\hat{\mathbf{H}}(s,f) = \mathbf{H}(s,f) / \sqrt{P_r(s,f)}$.

Fig. 16 shows the measured and simulated channel capacities of Route 1 Position 1 with 8 antennas at the Tx side, the ULA at the Rx side. We can notice that the simulation results show good agreements with the measurement results, which proves that the proposed general channel model is appropriate

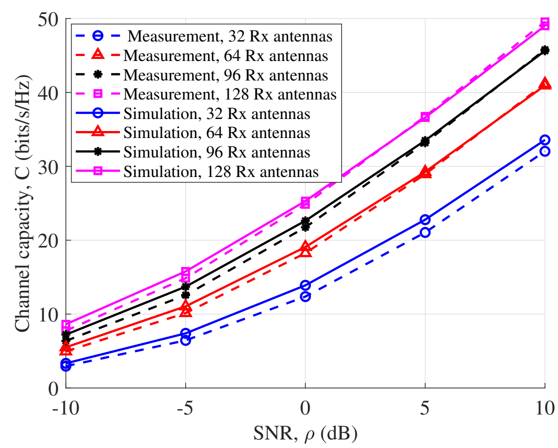


Fig. 16. The measured and simulated channel capacities of the single user in a NLOS environment for Route 1, Position 1, ULA ($\sigma_{ASA}$ = 12 m, $\sigma_{ASD}$ = 12 m, $\sigma_{ESA}$ = 10 m, $\sigma_{ESD}$ = 10 m, $\sigma_{DS}$ = 8 m, $\lambda^G$ = 20/m, $\lambda^R$ = 1/m).

for the measurement scenario. Furthermore, the SNR value has great influence on the channel capacity and large SNR value will increase the channel capacity. Under the premise of acceptable complexity, we can increase the number of antennas to increase channel capacity.

## V. Conclusions

In this paper, 5.3 GHz ultra-massive MIMO channel measurements with different antenna configurations have been conducted in an urban scenario. The statistical properties, including delay PSD, angular PSD, SCCF, normalized user-side correlation matrix, SVS, DoF, and diversity level have been investigated. The continuous variation of delay PSDs has illustrated spatial consistency and temporal non-stationarity properties. The mean values and variances of RMS DS and RMS AS have been shown to follow lognormal distributions. The difference between SCCFs in LOS and NLOS environments has indicated that the coherence distance in LOS environments is larger than that in NLOS environments. The variation range of AAoA of LOS path along the array when the Rx uses the DULA is larger than that of using the ULA, which has shown that the spherical wavefront is more evident for the longer antenna array. The correlation between users decreases with the increase of Rx antenna number, which has verified channel hardening characteristic. The correlation between users when the Rx uses the DULA is smaller than that of using the ULA in a LOS environment. We can conclude that the user correlation has been deduced by the longer antenna array. In addition, the values of DoFs and diversity are much smaller than the upper bound value $M_R \cdot M_T = 128 \times 8$, which clearly indicates the sparse property.

In addition, a general 3D non-stationary GBSM for 6G ultra-massive MIMO communication systems has been proposed. The proposed model has the ability to support multiple frequency bands and multiple scenarios. The statistical properties of the simplified ultra-massive MIMO channel model have been studied and validated by measurement results, including RMS DS, RMS AS, and SCCF. Similarly, the channel capacity has been investigated and validated by measurement results, which has verified the proposed general channel model and its practicability.

## REFERENCES


[1] X.-H. You, C.-X. Wang, J. Huang, *et al.*, "Towards 6G wireless communication networks: Vision, enabling technologies, and new paradigm shifts," *Sci. China Inf. Sci.*, vol. 64, no. 1, Jan. 2021, doi: 10.1007/s11432-020-2955-6.

[2] C.-X. Wang, J. Huang, H. Wang, X. Q. Gao, X.-H. You, and Y. Hao, "6G wireless channel measurements and models: Trends and challenges," *IEEE Veh. Technol. Mag.*, vol. 15, no. 4, pp. 22–32, Dec. 2020.

[3] D. Tse and P. Viswanath, *Fundamentals of wireless communication*, 1st ed. Cambridge: University Press, 2005.

[4] E. Björnson, J. Hoydis, and L. Sanguinetti, "Massive MIMO networks: Spectral, energy, and hardware efficiency," *Foundations and Trends in Signal Processing*, vol. 11, no. 3, pp. 154–655, 2017.

[5] C. F. López, C.-X. Wang, and Y. Zheng, "A 3D non-Stationary wideband massive MIMO channel model based on ray-level evolution," *IEEE Trans. Commun.*, vol. 70, no. 1, pp. 621–634, Jan. 2022.

[6] C. F. López and C.-X. Wang, "A study of 2D non-stationary massive MIMO channels by transformation of delay and angular power spectral densities," *IEEE Trans. Veh. Technol.*, vol. 69, no. 12, pp. 14212–14224, Dec. 2020.

[7] Y. Xin, D. Wang, J. Li, H. Zhu, J. Wang, and X.-H. You, "Area spectral efficiency and area energy efficiency of massive MIMO cellular systems," *IEEE Trans. Veh. Technol.*, vol. 65, no. 5, pp. 3243–3254, May. 2016.

[8] Y. Yuan, R. He, B. Ai, *et al.*, "A 3D geometry-based THz channel model for 6G ultra massive MIMO systems," *IEEE Trans. Veh. Technol.*, vol. 71, no. 3, pp. 2251–2266, Mar. 2022.

[9] J. Wang, C.-X. Wang, J. Huang, H. Wang, X. Q. Gao, and Y. Hao, "A novel 3D non-stationary GBSM for 6G THz ultra-massive MIMO wireless systems," *IEEE Trans. Veh. Technol.*, vol. 70, no. 12, pp. 12312–12324, Dec. 2021.

[10] J. Wang, C.-X. Wang, J. Huang, H. Wang, and X. Q. Gao, "A general 3D space-time-frequency non-stationary THz channel model for 6G ultra-massive MIMO wireless communication systems," *IEEE J. Sel. Areas Commun.*, vol. 39, no. 6, pp. 1576–1589, June 2021.

[11] W. Li, L. Liu, C. Tao, Y. Lu, J. Xiao, and P. Liu, "Channel measurements and angle estimation for massive MIMO systems in a stadium," in *Proc. ICACT'15*, PyeongChang, Korea (South), July 2015, pp. 105–108.

[12] Y. Lu, C. Tao, and L. Liu, "Research on propagation characteristics of massive MIMO channel at 1.4725 GHz," in *Proc. IEEE VTC-Spring*, Sydney, NSW, Australia, June 2017, pp. 1–5.

[13] S. Wu, C.-X. Wang, e. H. M. Aggoune, M. M. Alwakeel, and X.-H. You, "A general 3D non-stationary 5G wireless channel model," *IEEE Trans. Commun.*, vol. 66, no. 7, pp. 3065–3078, July 2018.

[14] C.-X. Wang, J. Bian, J. Sun, W. Zhang, and M. Zhang, "A survey of 5G channel measurements and models," *IEEE Commun. Surveys Tuts.*, vol. 20, no. 4, pp. 3142–3168, 4th Quart. 2018.

[15] C. F. López and C.-X. Wang, "Novel 3D non-stationary wideband models for massive MIMO channels," *IEEE Trans. Wireless Commun.*, vol. 17, no. 5, pp. 2893–2905, May 2018.

[16] S. Sangodoyin, V. Kristem, C. U. Bas, *et al.*, "Cluster-based analysis of 3D MIMO channel measurement in an urban environment," in *Proc. IEEE MILCOM'15*, Tampa, FL, USA, Oct. 2015, pp. 744–749.

[17] S. Sangodoyin, V. Kristem, C. U. Bas, *et al.*, "Cluster characterization of 3-D MIMO propagation channel in an urban macrocellular environment," *IEEE Trans. Wireless Commun.*, vol. 17, no. 8, pp. 5076–5091, Aug. 2018.

[18] X. Gao, O. Edfors, F. Rusek, and F. Tufvesson, "Massive MIMO performance evaluation based on measured propagation data," *IEEE Trans. Wireless Commun.*, vol. 14, no. 7, pp. 3899–3911, July 2015.

[19] X. Gao, F. Tufvesson, O. Edfors, and F. Rusek, "Measured propagation characteristics for very-large MIMO at 2.6 GHz," in *Proc. ASILOMAR'12*, Pacific Grove, CA, USA, Nov. 2012, pp. 295–299.

[20] X. Gao, M. Zhu, F. Rusek, F. Tufvesson, and O. Edfors, "Large antenna array and propagation environment interaction," in *Proc. ACSSC'14*, Pacific Grove, CA, USA, Nov. 2014, pp. 666–670.

[21] X. Gao, F. Tufvesson, and O. Edfors, "Massive MIMO channels–measurements and models," in *Proc. ASILOMAR'13*, Pacific Grove, CA, USA, Nov. 2013, pp. 280–284.

[22] S. Payami and F. Tufvesson, "Channel measurements and analysis for very large array systems at 2.6 GHz," in *Proc. EUCAP'12*, Prague, Czech Republic, Mar. 2012, pp. 433–437.

[23] S. Payami and F. Tufvesson, "Delay spread properties in a measured massive MIMO system at 2.6 GHz," in *Proc. PIMRC'13*, London, UK, Sept. 2013, pp. 53–57.

[24] Y. Zheng, L. Yu, R. Yang, and C.-X. Wang, "A general 3D non-stationary massive MIMO GBSM for 6G communication systems," in *Proc. IEEE WCNC'21*, Nanjing, China, Apr. 2021, pp. 1–6.

[25] S. Wu, C.-X. Wang, e. H. M. Aggoune, M. M. Alwakeel, and Y. He, "A non-stationary 3-D wideband twin-cluster model for 5G massive MIMO channels," *IEEE J. Sel. Areas Commun.*, vol. 32, no. 6, pp. 1207–1218, June 2014.

[26] S. Wu, C.-X. Wang, H. Haas, e. H. M. Aggoune, M. M. Alwakeel, and B. Ai, "A non-stationary wideband channel model for massive MIMO communication systems," *IEEE Trans. Wireless Commun.*, vol. 14, no. 3, pp. 1434–1446, Mar. 2015.

[27] J. Bian, C.-X. Wang, X. Q. Gao, X.-H. You, and M. Zhang, "A general 3D non-stationary wireless channel model for 5G and beyond," *IEEE Trans. Wireless Commun.*, vol. 20, no. 5, pp. 3211–3224, May 2021.

[28] L. Bai, Z. Huang, Y. Li, and X. Cheng, "A 3D cluster-based channel model for 5G and beyond vehicle-to-vehicle massive MIMO channels," *IEEE Trans. Veh. Technol.*, vol. 70, no. 9, pp. 8401–8414, Sept. 2021.

[29] H. Q. Ngo, E. G. Larsson, and T. L. Marzetta, "Aspects of favorable propagation in massive MIMO," in *Proc. EUSIPCO'14*, Lisbon, Portugal, Sept. 2014, pp. 76–80.

[30] P. Zhang, J. Chen, X. Yang, N. Ma, and Z. Zhang, "Recent research on massive MIMO propagation channels: A survey," *IEEE Commun. Mag.*, vol. 56, no. 12, pp. 22–29, Dec. 2018.

[31] J. Chen, "When does asymptotic orthogonality exist for very large arrays?" in *Proc. IEEE GLOBECOM'13*, Atlanta, GA, USA, Dec. 2013, pp. 4146–4150.

[32] J. Xi, J. Zhang, L. Tian, and Y. Wu, "Capacity analysis based on channel measurements of massive MU-MIMO system at 3.5 GHz," in *Proc. IEEE ICCC'17*, Chengdu, China, Dec. 2017, pp. 79–83.

[33] C. Wang, J. Zhang, L. Tian, M. Liu, and Y. Wu, "The variation of clusters with increasing number of antennas by virtual measurement," in *Proc. EUCAP'17*, Paris, France, Mar. 2017, pp. 648–652.

[34] À. O. Martínez, E. D. Carvalho, and J. Ø. Nielsen, "Massive MIMO properties based on measured channels: Channel hardening, user decorrelation and channel sparsity," in *Proc. ACSSC'16*, Pacific Grove, CA, USA, Nov. 2016, pp. 1804–1808.

[35] À. O. Martínez, J. Ø. Nielsen, E. D. Carvalho, and P. Popovski, "An experimental study of massive MIMO properties in 5G scenarios," *IEEE Trans. Antennas Propag.*, vol. 66, no. 12, pp. 7206–7215, Dec. 2018.

[36] Y. Xie, B. Li, X. Zuo, M. Yang, and Z. Yan, "A 3D geometry-based stochastic model for 5G massive MIMO channels," in *Proc. QSHINE'15*, Taipei, Aug. 2015, pp. 216–222.

[37] J. Li, B. Ai, R. He, M. Yang, Z. Zhong, and Y. Hao, "A cluster-based channel model for massive MIMO communications in indoor hotspot scenarios," *IEEE Trans. Wireless Commun.*, vol. 18, no. 8, pp. 3856–3870, Aug. 2019.

[38] X. Cai, B. Peng, X. Yin, and A. P. Yuste, "Hough-transform-based cluster identification and modeling for V2V channels based on measurements," *IEEE Trans. Veh. Technol.*, vol. 67, no. 5, pp. 3838–3852, May 2018.

[39] A. M. Sayeed, "Deconstructing multiantenna fading channels," *IEEE Trans. Signal Process.*, vol. 50, no. 10, pp. 2563–2579, Oct. 2002.

[40] J. Huang, C.-X. Wang, R. Feng, J. Sun, W. Zhang, and Y. Yang, "Multi-frequency mmWave massive MIMO channel measurements and characterization for 5G wireless communication systems," *IEEE J. Sel. Areas Commun.*, vol. 35, no. 7, pp. 1591–1605, July 2017.

[41] K. I. Pedersen, B. H. Fleury, and P. E. Mogensen, "High resolution of electromagnetic waves in time-varying radio channels," in *Proc. PIMRC'97*, Helsinki, Finland, Sept. 1997, pp. 650–654.

[42] X. Yin, L. Ouyang, and H. Wang, "Performance comparison of SAGE and MUSIC for channel estimation in direction-scan measurements," *IEEE Access*, vol. 4, pp. 1163–1174, 2016.

[43] 3GPP TR 38.901, "Study on channel model for frequencies from 0.5 to 100 GHz," 3GPP, Tech. Rep. Release 16, Dec. 2019.

[44] S. Jaeckel, L. Raschkowski, K. Börner, L. Thiele, F. Burkhardt, and E. Eberlein, "QuaDRiGa—Quasi Deterministic Radio channel Generator, user mannual and documentation," Fraunhofer Heinrich Hertz Institute, Tech. Rep. v2.4.0, 2020.

[45] K. Mammasis and P. Santi, "A two-dimensional geometry-based stochastic model," *IEEE Trans. Wireless Commun.*, vol. 11, no. 1, pp. 38–43, Jan. 2012.

[46] H. Jiang, M. Mukherjee, J. Zhou, and J. Lloret, "Channel modeling and characteristics for 6G wireless communications," *IEEE Netw.*, vol. 35, no. 1, pp. 296–303, Jan. 2021.

[47] Y. Liu, C.-X. Wang, J. Huang, J. Sun, and W. Zhang, "Novel 3-D nonstationary mmWave massive MIMO channel models for 5G high-speed train wireless communications," *IEEE Trans. Veh. Technol.*, vol. 68, no. 3, pp. 2077–2086, Mar. 2019.

[48] H. Chang, C. -X. Wang, Y. Liu, J. Huang, J. Sun, W. Zhang, and X. Q. Gao, "A novel nonstationary 6G UAV-to-ground wireless channel model with 3-D arbitrary trajectory changes," *IEEE Int. Things J.*, vol. 8, no. 12, pp. 9865–9877, June 2021.

[49] H. Jiang, Z. Zhang, J. Dang, and L. Wu, "A novel 3D massive MIMO channel model for vehicle-to-vehicle communication environments," *IEEE Trans. Commun.*, vol. 66, no. 1, pp. 79–90, Jan. 2018.

[50] H. Jiang, R. He, C. Ruan, J. Zhou, and D. Chang, "Three-dimensional geometry-based stochastic channel modeling for intelligent reflecting surface-assisted UAV MIMO communications," *IEEE Wireless Commun. Lett.*, vol. 10, no. 12, pp. 2727–2731, Dec. 2021.

[51] C.-X. Wang, Z. Lv, X. Q. Gao, X.-H. You, Y. Hao, and H. Haas, "Pervasive channel modeling theory and applications to 6G GBSMs for all frequency bands and all scenarios," *IEEE Trans. Veh. Technol.*, accepted for publication, doi: 10.1109/TVT.2022.3179695.

[52] M. Yang, B. Ai, R. He, *et al.*, "Non-stationary vehicular channel characterization in complicated scenarios," *IEEE Trans. Veh. Technol.*, vol. 70, no. 9, pp. 8387–8400, Sept. 2021.

[53] Z. Ma, B. Ai, R. He, *et al.*, "Impact of UAV rotation on MIMO channel characterization for air-to-ground communication systems," *IEEE Trans. Veh. Technol.*, vol. 69, no. 11, pp. 12418–12431, Nov. 2020.

[54] D. Gesbert, M. Shafi, D. Shiu, P. J. Smith, and A. Naguib, "From theory to practice: An overview of MIMO space-time coded wireless systems," *IEEE J. Sel. Areas Commun.*, vol. 21, no. 3, pp. 281–302, Apr. 2003.

[55] I. E. Telatar, "Capacity of multiantenna Gaussian channels," *Eur. Trans. Commun.*, vol. 10, no. 6, pp. 585–595, 1999.

[56] M. Matthaiou, M. R. Mckay, P. J. Smith, and J. A. Nossek, "On the condition number distribution of complex wishart matrices," *IEEE Trans. Commun.*, vol. 58, no. 6, pp. 1705–1717, June 2010.

[57] M. Matthaiou, A. M. Sayeed, and J. A. Nossek, "Sparse multipath MIMO channels: Performance implications based on measurement data," in *Proc. IEEE SPAWC'09*, Perugia, Italy, June 2009, pp. 364–368.

[58] H. Zhang, R. He, B. Ai, S. Cui, and H. Zhang, "Measuring sparsity of wireless channels," *IEEE Trans. Cogn. Commun. Netw.*, vol. 7, no. 1, pp. 133–144, Mar. 2021.

[59] R. He, B. Ai, G. Wang, M. Yang, C. Huang, and Z. Zhong, "Wireless channel sparsity: Measurement, analysis, and exploitation in estimation," *IEEE Wireless Commun.*, vol. 28, no. 4, pp. 113–119, Aug. 2021.

[60] A. Paier, T. Zemen, J. Karedal, *et al.*, "Spatial diversity and spatial correlation evaluation of measured vehicle-to-vehicle radio channels at 5.2 GHz," in *Proc. IEEE DSP'09*, Marco Island, FL, USA, Jan. 2009, pp. 326–330.

[61] J. Zhang, Y. Zhang, Y. Yu, R. Xu, Q. Zheng, and P. Zhang, "3-D MIMO: How much does it meet our expectations observed from channel measurements?" *IEEE J. Sel. Areas Commun.*, vol. 35, no. 8, pp. 1887–1903, Aug. 2017.


**Yi Zheng** received the B.Sc. degree from Dalian Maritime University, China, in 2016, and M.Eng. degree from Southeast University, China, in 2019.

She is currently pursuing the Ph.D. degree in the Nation Mobile Communications Research Laboratory, Southeast University, China. Her research interests include massive MIMO channel measurements and modeling and maritime communication channel characterization and modeling.

**Cheng-Xiang Wang** (Fellow, IEEE) received the B.Sc. and M.Eng. degrees in communication and information systems from Shandong University, China, in 1997 and 2000, respectively, and the Ph.D. degree in wireless communications from Aalborg University, Denmark, in 2004.

He was a Research Assistant with the Hamburg University of Technology, Hamburg, Germany, from 2000 to 2001, a Visiting Researcher with Siemens AG Mobile Phones, Munich, Germany, in 2004, and a Research Fellow with the University of Agder, Grimstad, Norway, from 2001 to 2005. He has been with Heriot-Watt University, Edinburgh, U.K., since 2005, where he was promoted to a Professor in 2011. In 2018, he joined Southeast University, Nanjing, China, as a Professor. He is also a part-time Professor with Purple Mountain Laboratories, Nanjing. He has authored 4 books, 3 book chapters, and more than 480 papers in refereed journals and conference proceedings, including 27 highly cited papers. He has also delivered 24 invited keynote speeches/talks and 14 tutorials in international conferences. His current research interests include wireless channel measurements and modeling, 6G wireless communication networks, and electromagnetic information theory.

Dr. Wang is a Member of the Academia Europaea (The Academy of Europe), a Member of the European Academy of Sciences and Arts (EASA), a Fellow of the Royal Society of Edinburgh (FRSE), IEEE, IET, and China Institute of Communication (CIC), an IEEE Communications Society Distinguished Lecturer in 2019 and 2020, and a Highly-Cited Researcher recognized by Clarivate Analytics in 2017-2020, and one of the most cited Chinese Researchers recognized by Elsevier in 2021. He is currently an Executive Editorial Committee Member of the IEEE TRANSACTIONS ON WIRELESS COMMUNICATIONS. He has served as an Editor for over ten international journals, including the IEEE TRANSACTIONS ON WIRELESS COMMUNICATIONS, from 2007 to 2009, the IEEE TRANSACTIONS ON VEHICULAR TECHNOLOGY, from 2011 to 2017, and the IEEE TRANSACTIONS ON COMMUNICATIONS, from 2015 to 2017. He was a Guest Editor of the IEEE JOURNAL ON SELECTED AREAS IN COMMUNICATIONS, Special Issue on Vehicular Communications and Networks (Lead Guest Editor), Special Issue on Spectrum and Energy Efficient Design of Wireless Communication Networks, and Special Issue on Airborne Communication Networks. He was also a Guest Editor for the IEEE TRANSACTIONS ON BIG DATA, Special Issue on Wireless Big Data, and is a Guest Editor for the IEEE TRANSACTIONS ON COGNITIVE COMMUNICATIONS AND NETWORKING, Special Issue on Intelligent Resource Management for 5G and Beyond. He has served as a TPC Member, a TPC Chair, and a General Chair for more than 80 international conferences. He received 15 Best Paper Awards from IEEE GLOBECOM 2010, IEEE ICCT 2011, ITST 2012, IEEE VTC 2013Spring, IWCMC 2015, IWCMC 2016, IEEE/CIC ICCC 2016, WPMC 2016, WOCC 2019, IWCMC 2020, WCSP 2020, CSPS 2021, WCSP 2021, and IEEE/CIC ICCC 2022. Also, he received the 2020-2022 "AI 2000 Most Influential Scholar Award Honourable Mention" in recognition of his outstanding and vibrant contributions in the field of Internet of Things.

**Runruo Yang** received the B.Sc. degree from University of Electronic Science and Technology of China, in 2018.

She is currently pursuing the Ph.D. degree in the Nation Mobile Communications Research Laboratory, Southeast University, China. Her main research interests include massive MIMO channel modeling, integrated sensing and communication channel characterization and modeling.

**Long Yu** received the B.E. degree in communication engineering from Xiamen University, Xiamen, China, in 2019 and the M.Sc. degree in electronic and communication engineering from Southeast University, Nanjing, China, in 2022.

His research interests include massive MIMO and AI-based predictive channel modeling.

**Fan Lai** received the B.E. degree from Dalian Maritime University, Dalian, China, in 2015.

He is currently working towards the Ph.D. degree in the National Mobile Communications Research Laboratory, Southeast University, Nanjing, China. His research interests include massive MIMO channel measurements and modeling, beam domain channel modeling, and shortwave channel modeling.

**Jie Huang** (Member, IEEE) received the B.E. degree in Information Engineering from Xidian University, China, in 2013, and the Ph.D. degree in Information and Communication Engineering from Shandong University, China, in 2018.

From October 2018 to October 2020, he was a Postdoctoral Research Associate in the National Mobile Communications Research Laboratory, Southeast University, China, supported by the National Postdoctoral Program for Innovative Talents. From January 2019 to February 2020, he was a Postdoctoral Research Associate in Durham University, UK. He is currently an Associate Professor in the National Mobile Communications Research Laboratory, Southeast University, China and also a researcher in Purple Mountain Laboratories, China. His research interests include millimeter wave, THz, massive MIMO, reconfigurable intelligent surface channel measurements and modeling, wireless big data, and 6G wireless communications.

He received Best Paper Awards from WPMC 2016, WCSP 2020, and WCSP 2021. He has also delivered 6 Tutorials in IEEE/CIC ICCC 2021, IEEE PIMRC 2021, IEEE ICC 2022, IEEE VTC-Spring 2022, IEEE/CIC ICCC 2022, and IEEE VTC-Fall 2022.

**Rui Feng** (Member, IEEE) received the B.Sc. degree in Communication Engineering from Yantai University, China, in 2011, the M.Eng. degree in Signal and Information Processing from Yantai University, China, in 2014, and the Ph.D. degree in Communication and Information System from Shandong University, China, in 2018. From July 2018 to Sept. 2020, she was a lecture in Ludong University, China.

She is currently a Postdoctoral Research Associate in Purple Mountain Laboratories and Southeast University, China. Her research interests include (ultra-) massive MIMO channel modeling theory and beam domain channel modeling.

**Chao Wang** received the Ph.D. degree from Beijing University of Posts and Telecommunications, Beijing, China, in 2019.

He is currently a senior engineer in Huawei Technologies CO., LTD, Shanghai, China. His research fields include wireless channel measurements and modeling, signal processing, the design and optimization of codebook, etc.

**Chao Li** received the M.S. degree from Shanghai Institute of Microsystem and Information Technology in electronic engineering.

He is currently a senior engineer in Huawei Technologies CO., LTD and focuses on channel sounder system design, channel modeling, and related physical layer algorithm technology research.

**Zhimeng Zhong** (Senior Member, IEEE) received the B.E., M.S., and Ph.D. degrees from Xi'an Jiaotong University, Xi'an, China, in 2002, 2005, and 2008, respectively, all in electronic engineering.

He joined Huawei Technologies CO., LTD from 2009, and about 13 years experiences on wireless communication system research and development. In these years, he mainly focused on wireless channel measurement, channel modelling, and MIMO algorithm & system design. He is the team leader of wireless channel research in Huawei. He is the wireless channel research expert in Huawei. Especially, he was in charge of the 3GPP 5G channel model standardization work in Huawei, and gave contributions on 3GPP mmWave channel model, V2V channel model, and IIOT Channel model standardization. Recently, he also focused on massive MIMO algorithm design based on some special channel characteristics and machine learning technologies.